Exciton dynamics probe the energy structure of a quantum dot-in-a-well system: The role of Coulomb attraction and dimensionality

Mirco Kolarczik,* Nina Owschimikow,† Bastian Herzog, Florian Buchholz, Yücel I. Kaptan, and Ulrike Woggon
Institut für Optik und Atomare Physik, Technische Universität Berlin, Germany
(Received 2 March 2015; revised manuscript received 28 April 2015; published 10 June 2015)

We investigate the energy structure of a quantum dot-in-a-well system by tracing the population of optically created excitons in pump-probe experiments and numerical simulations. The combination of a zero-dimensional and a two-dimensional substructure in this system gives rise to crossed excitons, with the electron confined in the quantum dot and the hole in the quantum well. An analysis of a large set of experiments at low carrier density and variable extraction potential shows that excitons created with no excess energy remain Coulomb-coupled and equilibrate and diffuse as correlated pairs. Individual quantum dots reach their quasi thermal equilibrium after few picoseconds, spatial equilibration of the whole system is reached after 300 ps.

DOI: 10.1103/PhysRevB.91.235310 PACS number(s): 82.53.Mj, 78.67.Hc, 45.30.+s

I. INTRODUCTION

The conversion between optical and electrical signals in semiconductors proceeds via creation and annihilation of excitons. Excitons are correlated electron-hole pairs, which can give rise to an electromagnetic field by recombination or to an electric current by dissociation into their constituent parts. To optimize the efficiency of this process in either direction is a key pursuit of researchers developing semiconductor-based solar cells and detectors as well as those working on amplifiers and lasers.

The energy of excitons in semiconductors can be controlled by design of the material structure and composition [1]. Frequently, the active region of semiconductor devices is nanostructured into thin two-dimensional (2D) quantum wells (QWs), one-dimensional quantum wires, or even zero-dimensional quantum dots (QDs), which offer a certain flexibility of designing the spectrum, and at the same time ensure a high overlap of electron and hole wave functions [2–6]. In particular, the strong confinement offered by QDs is promising for a large quantum yield [7,8]. The active QDs in optoelectronic devices are immersed in a solid state environment, which adds a complex energy landscape above the lowest QD modes. Understanding and quantifying the influence of this structured continuum on the dynamics of excitons will allow to tailor escape and capture rates and thus optimize the performance of optoelectronic devices.

In this contribution, we address the dynamics on the spatial and energy scale of an exciton created by light with an energy resonant to the QD ground state (GS) in a quantum dot-in-a-well (DWELL) system at room temperature. In DWELL structures, the active QD layer is, in addition to its wetting layer, capped with a QW layer [9]. This QW helps to relax the strain induced by the lattice mismatch. DWELLs show superior performance as photodetectors [10,11], and faster capture rates as light-emitting devices, such as lasers and amplifiers [12,13], compared to pure QD layers. For short times, those systems may still show typical features of two-level systems [14–16], but yet in- and out-scattering processes between the QD and its surroundings as well as carrier diffusion [17–19] proceed on a much faster time scale than the radiative recombination [20,21]. An exciton during its lifetime thus samples a large part of the structure, in energy as well as in space. Interdot exchange in QD systems has been observed in the literature [22–31], but mostly in time-resolved luminescence or photoluminescence excitation spectroscopy with excitation into the GaAs bulk, which adds an excess energy by far exceeding the exciton binding energy. In contrast to these previous experiments, we pump and probe QD energy levels, the experimental conditions thus resembling the absorption in a photodetector. With the sample being kept at room temperature, exciton escape and diffusion are thermally activated.

We create excitons in the QD GS of an In(Ga)As-based DWELL structure by resonant optical excitation with an ultrashort laser pulse. The QD GS is chosen for its uniquely defined transition energy, and the laser power is kept low to avoid multiple excitations per QD. We then trace the time evolution of the QD GS population in pump-probe experiments (Sec. II). Resonant experiments show the population decay in the initially excited QD, and in off-resonant experiments the lateral coupling between QDs is observed. We find that in all investigated cases, the dynamics is very well described by a transition of excitons into a quasi thermal equilibrium (the full thermal equilibrium corresponding to recombined excitons). This is followed by a subsequent diffusion of thermally ejected carriers in the QW with a probability of recapture by the QDs. A rate equation model built with these assumptions yields excellent agreement simultaneously with resonant and off-resonant experiments (Secs. III and IV). The model incorporates excitons as well as unpaired electrons and holes. We find that the probability for the exciton to dissociate is low, and only at long times and low remaining signal levels a purely excitonic description diverges from the observations. This hints at the importance of Coulomb attraction for the dynamics of dilute excitations. A quantitative analysis of the initial thermalization process reveals the influence of another Coulomb-mediated process, namely the formation of "crossed excitons" (CEs), i.e., excitons formed by one carrier confined in the QD, with the conjugate carrier in a 2D or

*mirco.kolarczik@tu-berlin.de
†nina.owschimikow@physik.tu-berlin.de

bulk energy level, and bound to the QD by Coulomb attraction (Sec. V) [29,32–34]. Tuning these CEs in and out of resonance with QD and QW states is an important design parameter with a significant influence on the carrier escape and capture processes in QDs.

II. DEVICE CHARACTERIZATION AND EXPERIMENTAL METHOD

The structure used in our experiments is an In(Ga)As-based semiconductor optical amplifier (SOA). The active region contains 15 layers of self-assembled QDs grown by molecular beam epitaxy with a nominal QD density of $\rho_{QD} = 10^{11}$ cm^{-2}. The QDs are immersed in an InGaAs QW in a DWELL structure. The QD layers are separated by 33–35 nm thick GaAs barriers to prevent vertical coupling. The active region is enclosed between p and n doped bulk GaAs (pin structure), the diode structure is illustrated in Fig. 1(a). The lateral extension of the active region is 2 μm, the length of the waveguide is 1.5 mm. A forward bias U_{ext} can be applied by a voltage supply connected to the device, reducing the built-in band offset $U_{int} = 855$ mV to a resulting extraction potential $U = U_{int} - U_{ext}$. Above the threshold given by $U = 0$ V, electrical carrier injection starts. In this contribution, all time-resolved experiments are conducted below threshold and current injection is only used for state characterization by amplified spontaneous emission (ASE), as shown in Fig. 1(b). In addition to the ground state (GS), energetically centered at 0.969 eV (1280 nm), the QDs exhibit one excited state (ES), which causes a second strong emission peak centered at 1.038 eV (1195 nm). Both GS and ES luminescence display a broadening of about 30 meV full width at half maximum (FWHM) due to the inhomogeneous size and shape distribution of the QDs. In addition to the direct QD excitons, the energy-level scheme in Fig. 1(a) shows also the positions of possible CEs assuming an energy level spacing for the valence band reduced by a factor of $a_{VB} = 2.7$ (Ref. [34]). The subscripts e and h denote electrons and holes, respectively.

In the time-resolved experiments, we use a heterodyne detected two-color pump-probe scheme [35]. Pump and probe pulses are derived from the two independently tunable amplifiers of a Toptica FemtoFiber Pro laser system running with a repetition rate of 75.4 MHz. In each of these amplifiers, the fundamental of an erbium-doped fiber oscillator is spectrally broadened into a supercontinuum, from which portions are selected by an amplitude mask in the Fourier plane of $4f$ pulse shapers, and compressed to a pulse duration of about 250 fs FWHM duration. Figure 1(c) shows the spectra of the pump pulses for the resonant and the off-resonant experiment as hatched and cross-hatched area, respectively, together with Gaussian distributions of the densities of states for the states overlapping with the optical excitation (GS and CE_6).

Prior to coupling into the device, the probe laser beam is split into a probe and a reference beam in an acousto-optic modulator (AOM), shifting the frequency of every laser mode of the probe beam by 77.3 MHz. After passing through the sample, the probe beam is interfered with the reference beam on a balanced photoreceiver (New Focus model 2117-FS), and the resulting slow beating at 1.9 MHz is detected by a fast lock-in amplifier (Perkin Elmer DSP

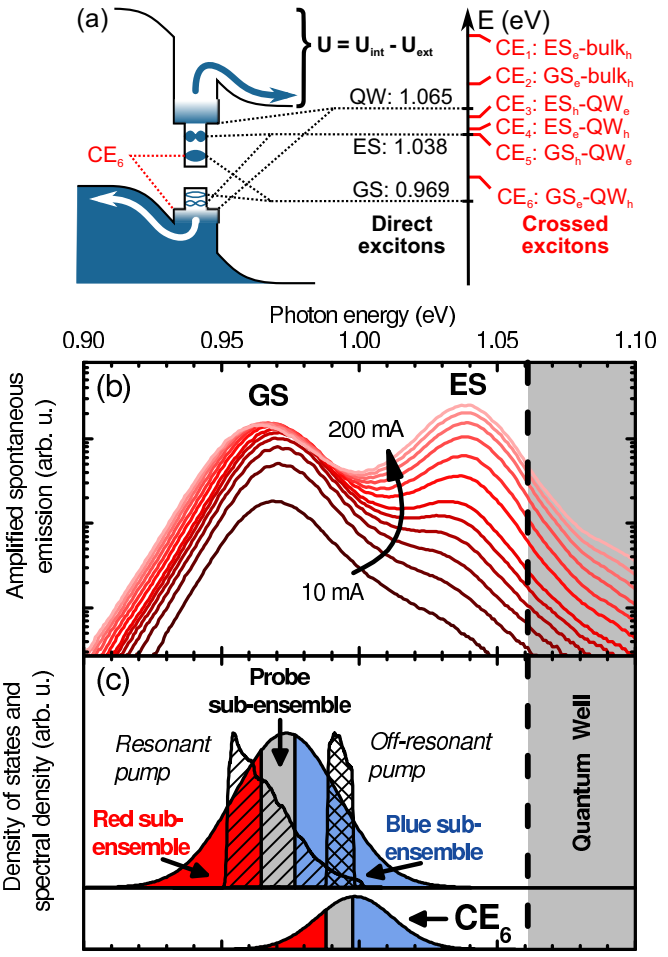

FIG. 1. (Color online) (a) Schematic of the DWELL structure within the diode structure with extraction potential U. Direct and crossed exciton transitions are indicated with their respective energies. (b) Amplified spontaneous emission with GS and ES emission, the dashed vertical line marks the QW band edge. (c) Density of states for the QD GS and CE_6 as assumed in the numerical model. Only CE_6, the CE with lowest energy, overlaps significantly with the pump spectra and contributes to the optical excitation. The probe subensemble boundaries are chosen according to the experimental probe spectra (not shown). The pump spectra (hatched and cross-hatched areas for resonant and off-resonant pump, respectively) determine the initial population.

7280). A schematic of the experimental setup is shown in Fig. 2(a).

Fast data acquisition using a National Instruments PCI 6251 DAQ card allows us to record real and imaginary parts of the lock-in signal at a rate of 10 kHz. By the same DAQ card and synchronized to the acquisition, the pump laser power can be rapidly switched by means of an AOM. Beyond switching the pump on and off, gradual switching allows to take simultaneous multi-power measurements (SMPM). With the high data acquisition rate, while the pump delay stage is continuously running, we typically track pump-probe traces at five SMPM power levels within 30 s, minimizing the susceptibility to slow drifts. By SMPM, we can monitor the saturation behavior and linearity of the sample response for all experimental conditions. In particular, we can exclude a

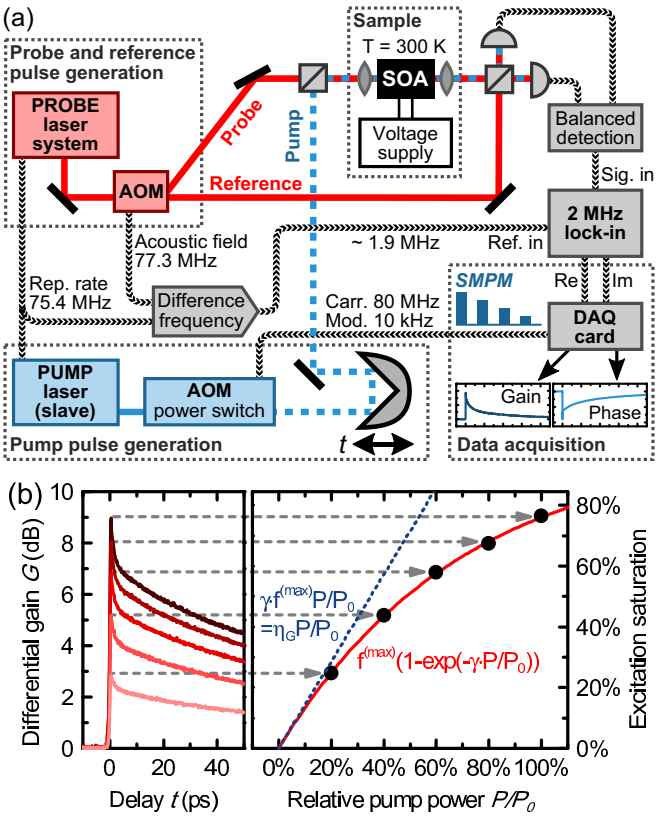

FIG. 2. (Color online) (a) The heterodyne pump-probe setup. The synchronized AOM control and data acquisition via DAQ card allows for fast sampling and simultaneous multipower measurements (SMPM). (b) (Left) An exemplary set of data, taken from the resonant series at $U = 750$ mV. (Right) A plot of peak amplitude versus pump power (level visualized by dashed arrows) shows a saturation well described by Eq. (1). In the low-power limit, the optical GS response increases linearly with $\eta_G = \gamma f^{(\max)}$ [dotted (blue) line].

significant influence of nonlinear processes like two-photon absorption on our experiments.

We base our data analysis on the differential gain $G(t)$. It is defined as $G_P(t) = 10\lg|S_P(t)/S_{\text{off}}(t)|$ in decibel (dB), where $S_P(t)$ is the lock-in signal with a pump pulse of power P, $S_{\text{off}}(t)$ is the signal without pumping, and t denotes the temporal delay of pump and probe pulse. Since the logarithm takes into account the effect accumulation upon propagation, $G(t)$ is proportional to the carrier population within the spectral range of the probe pulse. An exemplary SMPM set of differential gain curves is shown in Fig. 2(b). Positive values indicate increased gain, i.e., reduced absorption by creation of additional carriers by the pump pulse. With linearly increasing pump power, the data show a clear saturation behavior that is well-described by the function

$$f^{(\text{sat})}(P) = f^{(\max)}[1 - \exp(-\gamma P/P_0)] \qquad (1)$$

with $f_{\max} = (11.8 \pm 0.3)$ dB, $\gamma = 1.43 \pm 0.06$; and the maximum power $P_0 = 1.35$ mW (18.0 pJ/pulse) for this particular experiment. This dependence is visualized in Fig. 2(b) and used later to fit the optical GS response η_G (see Sec. IV E).

We performed two series of pump-probe experiments. Maximum power and spectral ranges are summarized in Table I, the pump pulse spectra are shown in Fig. 1(c). The probe pulse spectra (not shown) are restricted in width to the central area of the Gaussian distribution in Fig. 1(c) denoted as probe subensemble. In the first series, pump and probe spectra overlap. We will refer to this as the "resonant series." For the second pump-probe series, the "off-resonant series," the pump is centered at 0.993 eV (1249 nm) and separated from the probe by 13 meV [Fig. 1(c)]. Both series were repeated for a range of different forward bias voltages U_{ext}. To keep the experimental conditions as clean as possible, we varied U_{ext} between 0 and 850 mV, where the band bending is compensated. At higher bias, current starts to flow, and the additional heating and Coulomb interaction require a treatment on a higher level of complexity [19,36–38].

TABLE I. Parameters of the two experimental series, resonant and off-resonant, respectively. Spectrum limits denote energies at which the spectral density drops below 5% of the maximum value. The spectral distribution of the pump pulses is illustrated in Fig. 1(c).

Parameter	Resonant	Off-resonant
Maximum power P_0	1.35 mW	128 μW
Probe spectrum red limit	964 meV	965 meV
Probe spectrum blue limit	977 meV	975 meV
Pump spectrum red limit	951 meV	988 meV
Pump spectrum blue limit	998 meV	998 meV
Number of bias levels	18	22
Number of SMPM power levels	5	4
Total number of curves	90	88

III. RESULTS

Representative experimental results for the resonant and the off-resonant pump-probe series are shown as (blue) scatter plots in Figs. 3 and 4, respectively. The results of our numerical model, which is described in detail below, are shown as dashed (red) lines.

For the resonant series, we recorded a total of 90 pump-probe traces at 18 extraction potential steps with 5 SMPM levels in power. Figure 3(a) displays the differential gain G versus pump-probe delay t for different extraction potentials U from 0 to 750 mV for the resonant experimental series. We observe an ultrafast subpicosecond response, the amplitude of which increases with increasing U. A part of the initial response decays on a time scale of few ps, followed by a slower decay back to equilibrium. To visualize the long-time dynamics, the curves are displayed on a semilogarithmic scale in Fig. 3(b) for a longer time range. We see an almost single-exponential decay for high U, which changes to a transition between two time regimes with decreasing U. The ultrafast dynamics, on the other hand, is not sensitive to U, as is shown in Fig. 3(c), where we plotted the curves normalized to their maximum.

Analogous data and numerical simulation results for the off-resonant pump-probe series are collected in Figs. 4(a)–4(c). Here, we collected altogether 88 curves at 22 extraction potential steps and 4 SMPM power levels. For this series, the pump pulse was centered at 1249 nm, on the blue wing of the GS ASE distribution. Even though the spectral overlap of

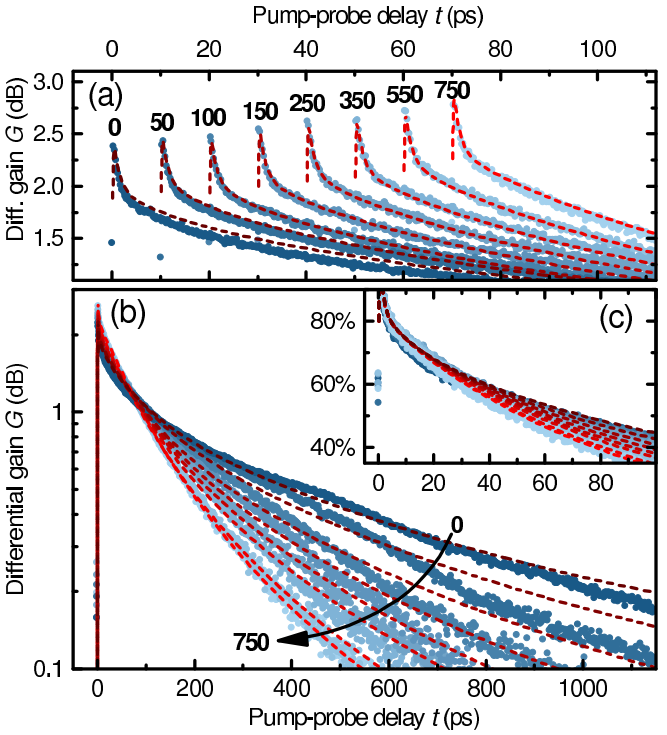

FIG. 3. (Color online) A representative set of data from the resonant series (20% of maximum power). The (blue) dots represent experimental data, the (red) dashed lines numerical fits, bold numerals in (a) and the arrow in (b) indicate extraction potential U (mV). (a) The initial decay of the gain curves shows little dependence on the extraction potential U. The data are displayed with a 10-ps horizontal offset for clarity. (b) Decay of differential gain on the nanosecond time scale. The long time dynamics strongly depend on U. (c) Gain curves normalized to the simulated curve maximum. The ultrafast dynamics is independent of U.

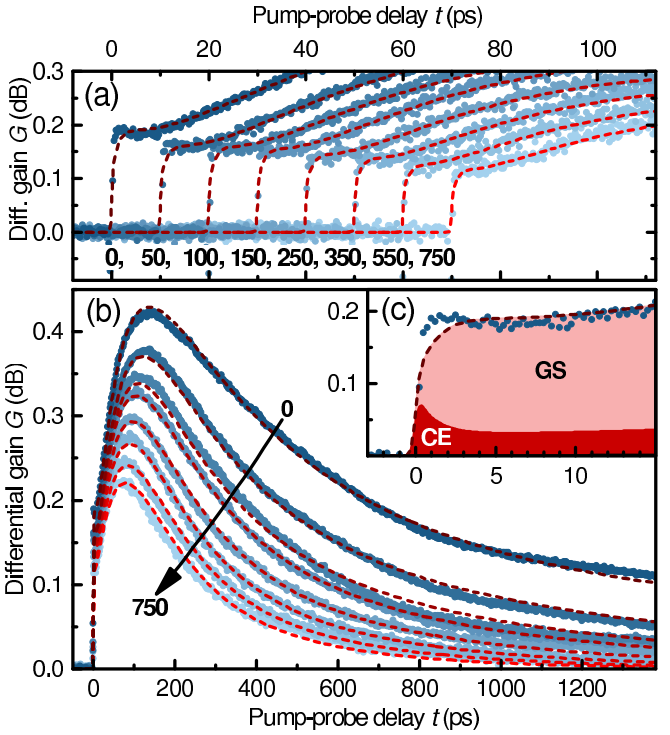

FIG. 4. (Color online) Off-resonant experiment (100% of maximum power), bold numerals in (a) and the arrow in (b) indicate extraction potential U (mV). The (blue) dots represent experimental data, the (red) dashed lines numerical fits. (a) Within the first few picoseconds, an immediate response is observed. Diffusing carriers arrive after some tens of picoseconds. (b) On the nanosecond time scale, diffusing carriers feed the probed GS, a maximum is reached at 137 ps for low extraction (dark curves). After 300 ps, the spatial inhomogeneity is smoothed out and the decay is similar to the resonant case (Fig. 3). (c) The contributions of GS and CE population according to the numerical model for $U = 0V$.

pump and probe pulses was negligible, we observe an ultrafast response and hints of an ultrafast decay in the probed QD GS at 1280 nm in all cases [Fig. 4(a)]. On an intermediate time scale, the pump-probe traces differ significantly from the resonant experiment. We observe a building up of population for about 100 ps, followed by a slow decay towards equilibrium [Fig. 4(b)]. All 178 curves can be excellently described in a simultaneous fitting procedure over three orders of magnitude in time and two orders of magnitude in signal amplitude.

IV. NUMERICAL MODEL

For a quantitative analysis of the data, we construct a rate equation model composed of the QD and a surrounding 2D continuum. A direct comparison in Refs. [23] and [39] of QDs with surrounding QW and such without even a wetting layer showed the decisive role of the QW in the interdot coupling. The qualitative change of decay behavior upon variation of the extraction potential U observed in Fig. 3(b) can be displayed in terms of an instantaneous time constant $\tau(t) = -G(t)/\dot{G}(t)$ [Fig. 5(a)]. It shows a constant decay rate for high U and a linear growth of the time constant for low extraction. This linear growth is expected for diffusive processes. We assume, without knowing the particular transfer mechanism, that the effective mathematical form of the carrier motion in 2D is the one of a diffusion process. We thus model the QD as a three-level system, and for the QW we assume an unstructured continuum in which we implement a random walk process for the particles with Boltzmann-distributed thermal velocities. The model is schematically displayed in Fig. 5(b).

We use a linear differential equation system

$$\frac{\mathrm{d}}{\mathrm{d}t}\vec{N} = M \cdot \vec{N} \tag{2}$$

with state vector $\vec{N}$ and a transition matrix M. If the matrix M is known, the solution $\vec{N}(t)$ can be easily calculated by numerical determination of the eigenvalues and eigenvectors of M. While this approach would not be sufficient to describe a QD-SOA in general, the specific experimental conditions described above make it applicable; here, every excitation is created in the GS of a spatially isolated QD, for most quantum dots a single exciton or no exciton at all is created (random biexcitons will be neglected). In this case, excitations are very dilute and exciton-exciton interactions can be neglected. Most of all, the absence of other carriers allows to treat fermions like bosons, without concerns about state filling. The calculations are carried out using SCILAB 5.5.1.

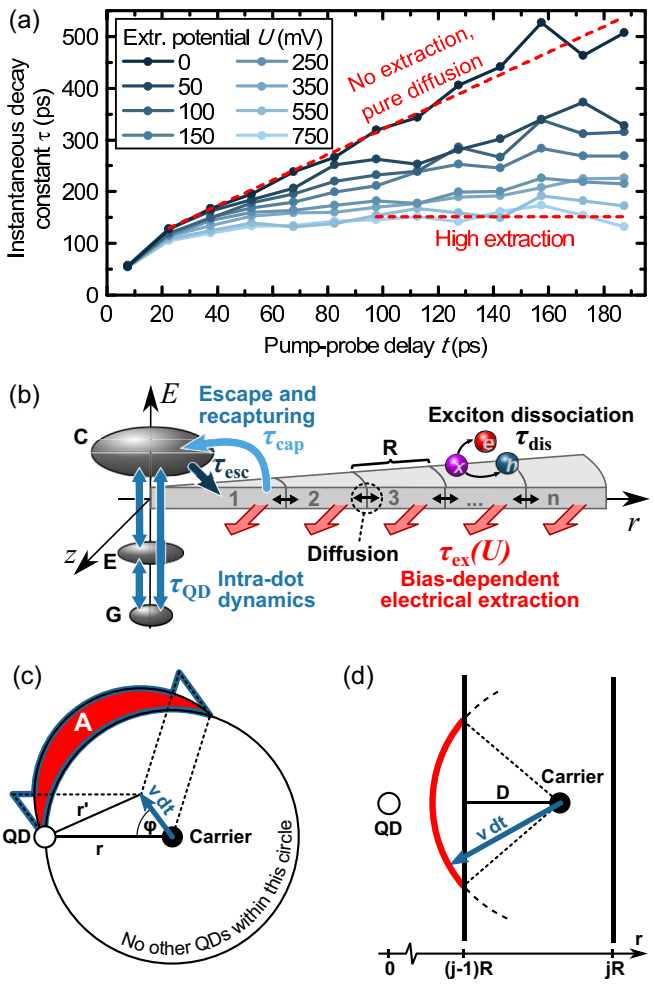

FIG. 5. (Color online) (a) Instantaneous decay constants $\tau(t) = -G(t)/\dot{G}(t)$ for the resonant pump-probe series at different extraction potentials, calculated from linear fits for 15-ps time intervals. The dashed (red) lines represent linear fits of the limiting cases of zero and high extraction. (b) The basic scheme of states for the rate equation model. (c) The transition probability to other QDs is proportional to the number of QDs in area A, which is approximated in Eq. (13) as the area with a bold (blue) contour. (d) Inward diffusion probability within one subensemble is proportional to the solid (red) fraction of the circle.

A. States

The fundamental scheme of the rate equation model and the allowed transitions between the states are illustrated in Fig. 5(b). The scheme is designed to take into account the spectral distribution of the states within the inhomogeneously broadened QD ensemble, different behavior of paired and unpaired carriers as well as different degrees of confinement. Instead of consecutive numbering we will use a triplet (jkl) to identify these three features, respectively, and to address the elements $N_{jkl,\xi}$ of $\vec{N}$, which is nevertheless a column vector. The fourth index $\xi \in \{\text{res},\text{off}\}$ for resonant and off-resonant experiment will only appear if it is necessary to distinguish between the two experimental series, and will be omitted otherwise for simplicity. For the elements of transition matrix M, we use the notation $M^{jkl}_{\iota\kappa\lambda}$ for the element in column (jkl) and row $(\iota\kappa\lambda)$, i.e., a transition from (jkl) to $(\iota\kappa\lambda)$ for positive entries. All elements of M not mentioned explicitly below are zero.

Confinement. By the first index $j \in \{\text{G},\text{E},\text{C},1,\ldots,n\}$ the quantum dot or 2D continuum state is identified. The QD is represented by a three-level scheme, containing the QD GS (G), the QD ES (E), and a generalized CE state (C). Note that the manifold of CE states available for equilibration contains all possible CE states, while the only CE state energetically accessible for optical excitation is the lowest state [CE_6, see Figs. 1(a) and 1(c)]. The numbered states represent the two-dimensional continuum into which the QD is embedded. In-plane radial symmetry allows to model the 2D continuum in a 1D representation; each of the n continuum states represents a ring of width R and outer radius jR, $j \in \{1,\ldots,n\}$, centered at the QD. The model for the continuum dynamics is explained in detail in Sec. IV C. The different states of the system have different degeneracy: while the sizes of ground state $N_{\text{G}}^{(\max)} = 1$ and excited state $N_{\text{E}}^{(\max)} = 2$ are fixed, the size of the crossed exciton state $N_{\text{C}}^{(\max)}$ is determined as a fit parameter. No specific size is attributed to continuum states, as explained below.

Spectral ensemble. The second index $k \in \{\text{r},\text{p},\text{b}\}$ identifies the relative energy of the spectral subensemble. Relative to the experimental probe pulse spectra, the QD ensemble is split into three subensembles [Fig. 1(c), details in Sec. IV E]. The central part of the QD ensemble is the probe subensemble (p), it represents a fraction of d_{p} of the QDs. QDs with lower GS energies are represented by the red subensemble (r) with size d_{r}, those with higher energies by the blue subensemble (b) with size d_{b}, with $d_{\text{r}} + d_{\text{p}} + d_{\text{b}} \equiv 1$. For the QD GS ensemble, we assume a Gaussian distribution for the density of states:

$$D(E) = \exp\left[-\ln 2\left(\frac{E - E^{(\text{ens})}}{w^{(\text{ens})}/2}\right)^2\right] \tag{3}$$

centered at $E^{(\text{ens})}$ and a FWHM of $w^{(\text{ens})}$ [see Fig. 1(c)].

Particle type. Finally, the particle type is given by the third index $l \in \{\text{x},\text{e},\text{h}\}$ for excitons (x), unpaired electrons (e) or unpaired holes (h). Of course, unpaired carriers cannot occupy CE states, so the state $j = \text{C}$ does not exist for $l \in \{\text{e},\text{h}\}$.

B. Transitions

Every state (jkl) is placed at a specific position E_{jkl} on the energy scale. The ground state energies of excitons ($j = \text{G}$, $l = \text{x}$) are determined as weighted average of the Gaussian ensemble distribution in Eq. (3). We assume $E_{\text{Ekx}} = E_{\text{Gkx}} + 70$ meV, which can be read directly from the ASE spectra [Fig. 1(b)] and

$$E_{\text{Ckx}} = E_{\text{Gkx}} + 100\ \text{meV}. \tag{4}$$

Equation (4) reflects the estimation of a weighted average for all CEs based on the knowledge that CE_1 and CE_2 exist above the QW band edge [34] and the assumption that CE_3-CE_6 [Fig. 1(a)] also provide states (see Sec. V for discussion). All continuum states are located at $E^{(\text{QW})} = 1.061$ eV, as was determined for a similar structure in Ref. [34]. For electrons and holes, ground and excited state energies ($j \in \{G,E\}$) are set to fulfill the condition $E_{jke} = (a_{\text{VB}}E_{jkx} + E^{(\text{QW})})/(a_{\text{VB}} + 1)$ and $E_{jkh} = (E_{jkx} + a_{\text{VB}}E^{(\text{QW})})/(a_{\text{VB}} + 1)$, respectively.

In our model, the probability for upward transitions ($E_{\iota\kappa\lambda} > E_{jkl}$) is reduced by the Boltzmann factor

$$\Delta^{jkl}_{\iota\kappa\lambda} = \exp\left(\frac{E_{jkl} - E_{\iota\kappa\lambda}}{k_\mathrm{B}T}\right) \tag{5}$$

with Boltzmann constant k_B and temperature $T = 300$ K. Downward transitions are not modified ($\Delta^{jkl}_{\iota\kappa\lambda} \equiv 1$ for $E_{\iota\kappa\lambda} \leqslant E_{jkl}$).

For intradot transitions between the states G, E, and C, we assume a time constant of $\tau_\mathrm{QD} = 2$ ps (Refs. [40,41]). The matrix elements for intradot transitions are under consideration of degeneracy:

$$M^{jlm}_{\iota lm} = N^{(\max)}_{\iota}\Delta^{jlm}_{\iota lm}\big/\tau_\mathrm{QD} \tag{6}$$

for $j,\iota \in \{\mathrm{G,E,C}\}, j \neq \iota$.

Transitions are allowed between the QD and continuum state 1. An exciton transits between QD state C and continuum state 1, so escape from the QD and capturing into the QD can be considered as a stepwise process only applying to one of the constituent carriers at a time, similar to the carrier capture via indirect excitons observed at elevated temperatures in Ref. [42]. A state size $N^{(\max)}$ is not introduced explicitly for the continuum and therefore the degeneracy is included in the time constants τ_esc for escape and τ_cap for capture, respectively. The matrix elements are given by

$$M^{1kx}_{Ckx} = \Delta^{1kx}_{Ckx}\big/\tau_\mathrm{cap}, \tag{7}$$

$$M^{Ckx}_{1kx} = \Delta^{Ckx}_{1kx}\big/\tau_\mathrm{esc}. \tag{8}$$

Since unpaired carriers $l \in \{\mathrm{e,h}\}$ do not have a CE state, the continuum state 1 is coupled to states G and E with the same time constants:

$$M^{1kl}_{jkl} = \Delta^{1kl}_{jkl}\left(\frac{N^{(\max)}_{j}}{N^{(\max)}_{\mathrm{G}} + N^{(\max)}_{\mathrm{E}}}\right)\Big/\tau_\mathrm{cap}, \tag{9}$$

$$M^{jkl}_{1kl} = \Delta^{jkl}_{1kl}\big/\tau_\mathrm{esc}. \tag{10}$$

for $j \in \{\mathrm{G,E}\}$.

C. Diffusion

In our model, we picture the lateral interdot carrier transfer as a consecutive process involving thermal ejection from a QD, subsequent diffusion in the QW, and capture by a QD. Tunneling between dots or the formation of QD molecules is unlikely at the given dot density, which corresponds to an average interdot distance of 30 nm [43,44]. The diffusion of carriers in the 2D continuum and the transition from one spectral subensemble to another is modeled in terms of simple geometrical considerations illustrated in Figs. 5(c) and 5(d). Carriers are treated as particles with masses $m_\mathrm{e} = m^*_\mathrm{e}$ for electrons, $m_\mathrm{h} = m^*_\mathrm{h}$ for holes and $m_\mathrm{x} = m_\mathrm{e} + m_\mathrm{h}$ for excitons, with the effective masses $m^*_\mathrm{e} = 0.041m_0$ for electrons and $m^*_\mathrm{h} = 0.465m_0$ for holes taken from the literature [45], with electron rest mass m_0. The particles move at thermal velocities given by the Boltzmann distribution

$$F_l(v)\mathrm{d}v\,\mathrm{d}\varphi = \frac{m_l v}{2\pi k_\mathrm{B}T}\exp\left(-\frac{m_l v^2}{2k_\mathrm{B}T}\right)\mathrm{d}v\,\mathrm{d}\varphi. \tag{11}$$

Every carrier is assigned to its nearest QD. Other QDs are assumed to be distributed homogeneously in the 2D continuum according to nominal QD density ρ_QD. A carrier transits from one QD to another if it is closer to a different QD after a motion of time interval $\mathrm{d}t$ [Fig. 5(c)]. In this moment, the distance to new and old nearest QD is equal, so the ring number j is conserved. The carrier starts at a distance r from its present QD in a direction given by angle φ to a new position at distance

$$\begin{aligned} r' &= \sqrt{(v\,\mathrm{d}t\,\sin\varphi)^2 + (r - v\,\mathrm{d}t\,\cos\varphi)^2} \\ &\approx \sqrt{r^2 - 2\,r\,v\,\mathrm{d}t\cos\varphi}, \end{aligned} \tag{12}$$

where we used $v\,\mathrm{d}t \ll r$. The transition probability is equal to the number of QDs in the (red) filled area A, which can be approximated as

$$\begin{aligned} A(r,v,\varphi) &= |\varphi|(r'^2 - r^2) + 2\,r\,v\,\mathrm{d}t\,|\sin\varphi| \\ &= 2\,r\,v\,\mathrm{d}t(|\sin\varphi| - |\varphi|\cos\varphi) \end{aligned} \tag{13}$$

with $\varphi \in [-\pi,\pi]$. By integrating over all directions and velocities, the transition matrix element becomes

$$\begin{aligned} M^{jkl}_{j\kappa l} &= d_\kappa\rho_\mathrm{QD}\int_{v=0}^{\infty}\int_{\varphi=-\pi}^{\pi}\mathrm{d}v\,\mathrm{d}\varphi\,F_l(v)\frac{A(r,v,\varphi)}{\mathrm{d}t} \\ &= d_\kappa\rho_\mathrm{QD}\sqrt{\frac{32\,k_\mathrm{B}T}{\pi m_l}}r \end{aligned} \tag{14}$$

with $k,\kappa \in \{\mathrm{r,p,b}\}, k \neq \kappa$ under consideration of subensemble size d_k.

To derive the probability to move inward from ring $j \in \{2,\ldots,n\}$ to the next inner ring $j-1$ within the same subensemble, we consider a carrier at distance D from the ring border [Fig. 5(d)]. The probability to cross the border is given by $p(v,D) = (\arccos\frac{D}{v\mathrm{d}t})/\pi$ for $D \leqslant v\,\mathrm{d}t$, and $p(v,D) \equiv 0$ otherwise. Integration over all velocities and points of the ring yields

$$\begin{aligned} M^{jkl}_{(j-1)kl} &= \frac{2(j-1)}{(2j-1)R\mathrm{d}t}\int_{v=0}^{\infty}\mathrm{d}v\,F_l(v)\int_{D=0}^{R}\mathrm{d}D\,p(v,D) \\ &= \frac{2(j-1)}{(2j-1)R}\sqrt{\frac{2\,k_\mathrm{B}T}{\pi m_l}}, \end{aligned} \tag{15}$$

where we used that the carrier distance from the QD is approximately constant at $(j-1)R$.

An analogous calculation yields the outward diffusion matrix element for $j \in \{1,\ldots,(n-1)\}$. Moving away from the nearest QD also increases the probability to reach the area of another QD. Since outward movement becomes inward movement from the viewpoint of the new QD in this case, we assume that a carrier that changes the subensemble actually does not diffuse outward any more, therefore we reduce the matrix element by the result from Eq. (14):

$$M^{jkl}_{(j+1)kl} = \frac{2j}{(2j-1)R}\sqrt{\frac{2\,k_\mathrm{B}T}{\pi m_l}} - \sum_{\kappa\neq k}M^{jkl}_{j\kappa l}. \tag{16}$$

This matrix element also determines the necessary number of rings n that is given by $M^{nkl}_{(n+1)kl} \leqslant 0$.

D. Extraction and decay

So far, only off-diagonal elements of M have been discussed. All the processes described above conserve the number of particles in the system. Additionally, we included several decay processes into the numerical model, which annihilate particles or dissociate excitons into unpaired carriers. First, excitons in all states are subject to recombination determined by an average recombination time constant τ_{rec}. Furthermore, excitons in the 2D continuum dissociate with a time constant τ_{dis} and create an unpaired electron and hole. In the continuum states, also the extraction potential U extracts unpaired carriers from the system and single carriers from excitons with a time constant τ_{ex}, the latter meaning the annihilation of an exciton and simultaneous creation of an unpaired carrier. Therefore we find another off-diagonal element for $l \in \{\mathrm{e,h}\}$ that represents intrinsic and potential-induced exciton dissociation, respectively, for continuum states $j \in \{1, \ldots, n\}$:

$$M_{jkl}^{jk\mathrm{x}} = \tau_{\mathrm{dis}}^{-1} + \tau_{\mathrm{ex}}^{-1}(U). \tag{17}$$

Thus, the diagonal-elements of exciton continuum states become

$$M_{jk\mathrm{x}}^{jk\mathrm{x}} = -\left(\sum_{(\iota\kappa\lambda)\neq(jk\mathrm{x})} M_{\iota\kappa\lambda}^{jk\mathrm{x}} \right) - \tau_{\mathrm{rec}}^{-1} + \tau_{\mathrm{dis}}^{-1}, \tag{18}$$

where the term in parentheses sums the corresponding off-diagonal elements for particle number conservation and the last term compensates the double appearance of the first term of Eq. (17) in this sum (two unpaired carriers are created by dissociation, but only one exciton is annihilated). For excitons $l = \mathrm{x}$ in quantum dot states $j \in \{\mathrm{G,E,C}\}$ only recombination applies:

$$M_{jk\mathrm{x}}^{jk\mathrm{x}} = -\left(\sum_{(\iota\kappa\lambda)\neq(jk\mathrm{x})} M_{\iota\kappa\lambda}^{jk\mathrm{x}} \right) - \tau_{\mathrm{rec}}^{-1}. \tag{19}$$

Unpaired carriers $l \in \{\mathrm{e,h}\}$ can not recombine, so extraction is the only decay channel in the continuum $j \in \{1, \ldots, n\}$:

$$M_{jkl}^{jkl} = -\left(\sum_{(\iota\kappa\lambda)\neq(jkl)} M_{\iota\kappa\lambda}^{jkl} \right) - \tau_{\mathrm{ex}}^{-1}(U) \tag{20}$$

and no decay channels apply for the quantum dot states $j \in \{\mathrm{G,E,C}\}$:

$$M_{jkl}^{jkl} = -\left(\sum_{(\iota\kappa\lambda)\neq(jkl)} M_{\iota\kappa\lambda}^{jkl} \right). \tag{21}$$

E. Optical interaction

As a last step, optical pumping and probing have to be implemented, where pumping means setting an initial state $\vec{N}_{\xi UP}^{(0)} = \vec{N}_{\xi UP}(t=0)$ and probing means the derivation of a gain curve $G_{\xi UP}(t)$ from the solution $\vec{N}_{\xi UP}(t)$ of Eq. (2) for every experimental series $\xi \in \{\mathrm{res,off}\}$, extraction potential U, and optical pump power P. The calculation is based on two parameters, the optical GS response η_{G} and the optical CE_6 response η_{C}, respectively. Both parameters are allowed to depend on U, η_{C} additionally depends on P, to reproduce the dependencies in the experimental transition probabilities. Table II summarizes the subsets of data used to determine η_{G} and η_{C}. If one of them is not determined explicitly for a curve, it is interpolated from the parameters of other curves.

The optical GS response η_{G} governs the peak height in the resonant experiment series [Fig. 2(b)]. According to Eq. (1), we determine $f_U^{(\max)}$ and γ_U from the SMPM power dependence of the resonant experiment series for every U. Since these fit parameters are strongly interdependent, we will discuss the product $\eta_{\mathrm{G},U} = \gamma_U f_U^{(\max)}$ as the optical GS response.

The model for the conversion of light to population follows the spectra shown in Fig. 1(c). The spectral limits of the probe subensemble, $\nu_{\mathrm{Gp},\xi}^{(\min)}$ and $\nu_{\mathrm{Gp},\xi}^{(\max)}$, are set where the spectral density of the probe pulse drops below 5% of the maximum value (see Table I). From the measured pump spectra we

TABLE II. Overview of model parameters. Except for the last three rows (explained in detail in Fig. 6), these parameters are used by all curves. The right-hand side of the table depicts fitting details: the fitting routine can be restricted to a certain subset of curves, to a time range $t_{\min} \leqslant t \leqslant t_{\max}$, and to upper and lower value limits. For values in parentheses, this limit has not been reached.

Parameter	Value	Experiment series	$t_{\min}$	$t_{\max}$	Lower limit	Upper limit
GS ensemble center $E^{(\mathrm{ens})}$	973.5 meV	Both	0 ps	∞	(971 meV)	(974.5 meV)
GS ensemble width (FWHM) $w^{(\mathrm{ens})}$	44.1 meV	Both	0 ps	∞	44.1 meV	(55.8 meV)
Ring width R	3 nm	(Fixed)				
CE state size $N_{\mathrm{C}}^{(\max)}$	25.9	Resonant	5 ps	15 ps	(0)	
Intra-dot time τ_{QD}	2 ps	(Fixed)				
Escape time τ_{esc}	16.5 ps	See Fig. 7(a)	50 ps	200 ps	(0 ps)	
Capture time τ_{cap}	49.2 fs	Both	0 ps	100 ps	(0 ps)	
Recombination time τ_{rec}	752 ps	Both	0 ps	∞	(0 ps)	
Dissociation time τ_{dis}	2500 ps	Both	0 ps	∞	(0 ps)	2500 ps
Optical GS response η_{G}	Fig. 6(a)	Resonant	0 ps	1.5 ps	(0)	
Optical CE_6 response η_{C}	Fig. 6(b)	Off-resonant	0 ps	10 ps	(0)	
Extraction time τ_{ex}	Fig. 6(c)	Both	0 ps	∞	(0 ps)	

derive the spectral photon density $\Phi_\xi(\nu)$. According to this distribution, the initial population is set to

$$N^{(0)}_{\mathrm{Gkx},\xi UP} = f_U^{(\max)} \int_{\nu^{(\min)}_{\mathrm{G}k,\xi}}^{\nu^{(\max)}_{\mathrm{G}k,\xi}} (1 - e^{-\gamma_U P \Phi_\xi(\nu)}) D(h\nu) \mathrm{d}\nu, \quad (22)$$

$$N^{(0)}_{\mathrm{Ckx},\xi UP} = \eta_{\mathrm{C},UP} \int_{\nu^{(\min)}_{\mathrm{C}k,\xi}}^{\nu^{(\max)}_{\mathrm{C}k,\xi}} P\Phi_\xi(\nu) \times D\left(\frac{(a_{\mathrm{VB}}+1)h\nu - E^{(\mathrm{QW})}}{a_{\mathrm{VB}}}\right) \mathrm{d}\nu, \quad (23)$$

where h is the Planck constant.

The differential gain for GS probing is calculated as a weighted sum of states from the solution $\vec{N}(t)$ of Eq. (2). Only carriers in the probe subensemble contribute to the weighting vector $\vec{W}$, the marginal overlap with CE_6 of the red subensemble [Fig. 1(c)] is neglected. Unpaired carriers in state G switch a QD in the probe subensemble from being absorbing to transparent; this contribution is set to $W_{\mathrm{Gpe}} = W_{\mathrm{Gph}} = 1$. Also, crossed excitons in state C of the probe subensemble may switch the GS transition to transparency, if one carrier of the CE is in a QD GS state. Here, we assume that 80% of CEs are related to a conduction or valence band GS (20% related to ES are not probed experimentally), so $W_{\mathrm{Cpx}} = 0.8$. An exciton in state G switches a QD from absorbing to amplifying, so it contributes with $W_{\mathrm{Gpx}} = 2$. Considering the bias-dependent optical GS response, the differential gain becomes

$$G_{\xi UP}(t) = \eta_{\mathrm{G},U}(\vec{W} \cdot \vec{N}_{\xi UP}(t)). \quad (24)$$

For comparison with experimental data, all simulated curves are convoluted with a Gaussian of 500 fs FWHM to take temporal resolution into account. The model parameters are summarized in Table II. They were fitted to the data by an iterative minimization of squares if not depicted otherwise in the table.

V. DISCUSSION

From our numerical simulation, we can now extract the underlying physical processes that are reflected in the pump-probe traces. In the resonant case, the excitation decays in three stages. Within the first 3 ps, the exciton distribution relaxes from the GS to a quasi thermal equilibrium [Fig. 3(a)]. This proceeds predominantly by intra-dot transitions to the ES and CE state governed by the time constant τ_{QD}. In the intermediate time regime (3 ps to 300 ps), we observe a strong dependence of the population decay on the extraction potential. For strong extraction, the decay becomes nearly single-exponential since the return probability for excitons that escaped from QDs is strongly reduced. For low extraction, the resulting decay rate decreases due to an increasing probability of recapture from the continuum. Finally, for $t > 300$ ps, the excitation is spatially equilibrated over the entire system and decays at a potential-dependent average rate. Nevertheless, we see a slight reduction of this rate for later times, especially in the high extraction case. As experiment and model agree very well in this aspect, this can be attributed to unpaired carriers that cannot recombine any more. Generally, in our observations, the dynamics is well described by carriers relaxing and diffusing as excitons, rather than as unpaired electrons and holes. In case of fast dissociation and diffusion of unpaired carriers, one would expect a strong dependence of the long time behavior on the initial carrier density increasing with the SMPM power level, as re-pairing is necessary for recombination. However, this is not observed. These findings are in contrast to results obtained in photoluminescence spectroscopy [22] with excitation into the bulk, where carriers were found to behave as independent electrons and holes. Creating carriers with no excess energy in our case maintains the Coulomb correlation, and leads to a dominating excitonic behavior.

The off-resonant experiment yields complementary information from the viewpoint of a spectrally—and as well spatially—different QD subensemble. An immediate response observed for short times indicates absorption by a CE state coupled to the GS of the QDs of the pumped spectral range [34]. According to the density of states scheme in Fig. 1(c), CE_6 of the probed subensemble is pumped in this case, leading to a direct response of the probed (off-resonant) subensemble [Fig. 4(a)]. Figure 4(c) visualizes the relative contributions of QD GS and all CEs according to Eq. (24). At longer times, diffusing excitons arrive in the probed subensemble and start filling the GS in the intermediate-time regime. The population maximum is reached after 137 ps for $U = 0$ V. In the long-time regime, the off-resonant experiment behaves like the resonant one due to spatial equilibration.

A deeper insight into the nature of the contributing transitions is gained from the dependence of the parameters presented in Fig. 6 on the extraction potential U and the pump power P. Of particular interest is the comparison of the optical GS response η_{G} [Fig. 6(a)] and the optical CE_6 response η_{C} [Fig. 6(b)] obtained from the numerical fits to the data. Remarkably, these transitions exhibit an opposite dependence on the extraction potential. While η_{G} is smallest for low U and increases continuously for increasing potential, the optical CE_6 response η_{C} is largest for compensated band bending and decreases for increasing U. This is a strong indication that GS and CE_6 are indeed different states, as the natural polarization of the QD-QW crossed exciton is shown in the literature [46] to be perpendicular to the QD GS transition, hence the opposite response to a polarizing electric field. The observed pump power dependence in Fig. 6(b) could be caused by an excitation-power dependent linewidth broadening of the GS transition [47], resulting in an increased spectral overlap of pump and probe pulse that becomes non-negligible compared to CE_6 for high power. The vertical offset thus can be attributed to unintended GS pumping.

The efficiency of carrier extraction is an important figure of merit for detectors and solar cells. We quantify it for our system through the parameter τ_{ex}^{-1}, which we determine for every curve [Fig. 6(c)]. The efficiency of extraction increases as the extraction potential aids the charge separation. Strong band bending thus means strong extraction. Interestingly, the extraction efficiency we observe shows at high U (low forward bias) also a pump power dependence. For increasing pump power, the data show a reduction of extraction efficiency. Two processes might contribute to this behavior: on one hand, two-photon absorption occurs for high optical power that dominates in the case of low electrical carrier injection (not shown), but is present also below threshold. The additional carriers

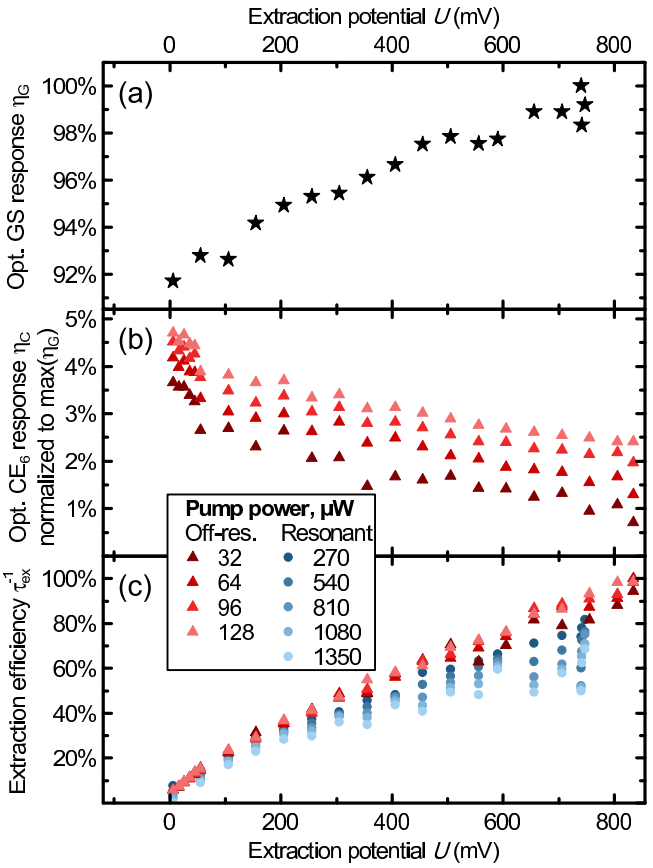

FIG. 6. (Color online) Parameters with potential and power dependence. (a) Normalized optical GS response $\eta_G = \gamma f^{(max)}$, with γ and $f^{(max)}$ according to Eq. (1) fit to the initial population of the resonant experiment. (b) Optical CE_6 response η_C, also normalized to the maximum of η_G. (c) Extraction efficiency τ_{ex}^{-1}. Efficiency reduction for high pump power can be attributed to compensating fields caused by a large number of extracted carriers.

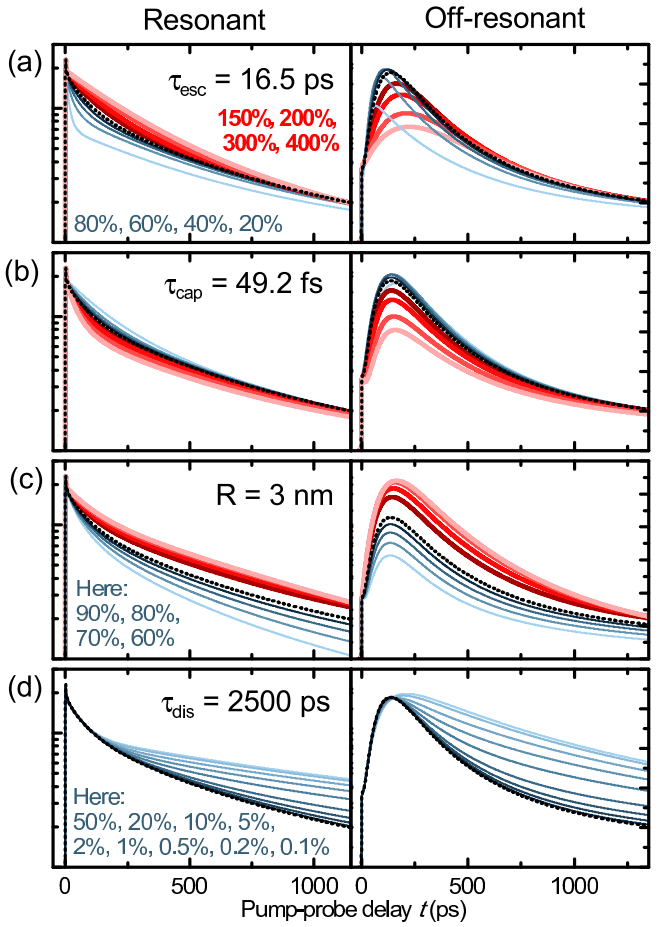

FIG. 7. (Color online) Variation of model parameters for the $U = 0$ V curves in Figs. 3 and 4 (data shown as dotted line). If not depicted otherwise, bold (red) curves represent increased values (150%, 200%, 300%, 400% from dark to light), thin (blue) curves represent decreased values (80%, 60%, 40%, 20% from dark to light). (a) Escape time τ_{esc} has crucial influence on the temporal position of the signal maximum in the off-resonant experiment. (b) For slow capturing (increased τ_{cap}) less carriers populate the QD states. (c) In contrast to τ_{esc} and τ_{cap}, the ring width R has a significant influence on the long time behavior. (d) Exciton dissociation to unpaired electrons and holes is found to be too slow to be observed clearly within the temporal range of our experiment. Faster decay would result in a long lasting signal component.

relaxing from higher states would compensate the extraction partially. On the other hand, and more important in our opinion, the larger number of created carriers for higher pump powers will intrinsically compensate the band bending and screen the extraction potential [48].

A systematic variation of model parameters in Fig. 7 reveals the influence of individual processes on the system dynamics. Parts (a)–(d) of the figure show calculations reproducing the curves measured for zero extraction potential (shown as dotted lines) from Figs. 3 and 4, and the results upon varying the given parameters. Thin (blue) curves represent decreased values of τ_{esc} [Fig. 7(a)], τ_{cap} [Fig. 7(b)], R [Fig. 7(c)], and τ_{dis} [Fig. 7(d)]. Bold (red) curves correspond to increased values, respectively.

Apart from the carrier number relations, the temporal development of the carrier population is defined primarily by escape time τ_{esc}, capture time τ_{cap} and ring width R. Variations of these parameters are displayed in Figs. 7(a)–7(c) for the resonant and the off-resonant series. These three parameters are interdependent within our model approach, so we cannot claim a physical significance for the numerical values our fitting procedure extracts. Furthermore, one must have in mind that τ_{esc} and τ_{cap} do not reflect just the wave-function overlap, but also include energy information according to Eq. (4), the state size ratio of state C and continuum state 1, and are determined for the QD-QW coupling model that neglects spatially extended coupling beyond continuum state 1. Thus the ratio $\tau_{esc}/\tau_{cap} = 335$ in Table II must be read with care. A variation of the individual parameters, however, provides a qualitative insight into the dynamics.

A first observation is the critical dependence of the temporal position of the signal maximum in the off-resonant series on τ_{esc}. We exploited this observation during the fitting process, where we used minimization of deviation from the experimental maximum (137 ps) instead of least squares for τ_{esc}. On the other hand, τ_{cap} and R affect the temporal

position less than the height of the maximum. In the resonant series, especially the steepness of decay after thermalization is determined by time constants τ_{esc} and τ_{cap}. These time constants have significant influence on the curve shape in the intermediate time range, but result in similar signal levels after 1 ns, when carriers have spread over the entire system. In contrast, the long time signal level is very susceptible to ring width R. The ring width in our model determines the number of scattering events a carrier in the continuum experiences, as any directional information of former steps is erased and independently redetermined by Eq. (11). Disorder thus induces localization.

The dissociation time constant τ_{dis} governs the survival of excitons. Its influence can be seen in Fig. 7(d). Faster dissociation means more electrons and holes without recombination possibilities that survive for a long time in the resonant and the off-resonant case.

VI. CONCLUSIONS

We observed the optically induced carrier dynamics in a quantum dot-in-a-well system at low carrier densities in two-color ultrafast pump-probe experiments at room temperature. QDs in a well represent a combined zero-dimensional and two-dimensional system, which in addition to the QD and QW eigenstates exhibits "crossed exciton" states, with one carrier confined in the QD and the conjugate carrier in the QW. The CEs are bound together by Coulomb attraction. Their influence is revealed on the ultrafast time scale by the presence of a transition channel feeding or depleting the QD GS, and having an energy corresponding to QW energy levels. Once escaped to the QW, in our observations the carriers are still likely to form correlated pairs, which are then re-captured by their original or a neighboring QD. To support these assumptions, we created a numerical model approach for inter-dot diffusion including CE states that simultaneously reproduces the temporal evolution of 178 pump-probe traces in two series of experimental data over three orders of magnitude in time and two orders of magnitude in amplitude. The model-based analysis of bias and power dependencies revealed significant differences in the optical response of the addressed direct and crossed excitons: while direct transitions are most efficient in the unbiased case, the crossed excitons show opposite behavior, supporting the assumption of two qualitatively different transitions. Coulomb effects and dimensionality together form a potential landscape, which prefers excitons over unpaired carriers and creates an additional trapping potential around the QDs. For a complete explanation the dynamics thus has to be analyzed on a spatial as well as on an energy scale. For the optimization of similar structures for device applications, the robustness of these effects in presence of carrier-carrier scattering at higher densities created by injection currents is of high interest.

ACKNOWLEDGMENTS

The device was fabricated by the group of Dieter Bimberg. Financial support was provided by Deutsche Forschungsgemeinschaft (DFG) via Sonderforschungsbereich 787 and the Research Training Group GRK 1558.

[1] G.-C. Yi, ed., *Semiconductor Nanostructures for Optoelectronic Devices* (Springer, Berlin, Heidelberg, 2012).
[2] H. Haug and S. W. Koch, *Quantum Theory of the Optical and Electronic Properties of Semiconductors* (World Scientific, Singapore, 1990).
[3] P. K. Bhattacharya and N. K. Dutta, Annu. Rev. Mater. Sci. **23**, 79 (1993).
[4] H. Sakaki, Surface Sci. **267**, 623 (1992).
[5] F. Lelarge *et al.*, IEEE J. Select. Top. Quantum Electron. **13**, 111 (2007).
[6] P. Bhattacharya, S. Ghosh, and A. D. Stiff-Roberts, Annu. Rev. Mater. Res. **34**, 1 (2004).
[7] *Nano-Optoelectronics*, edited by M. Grundmann (Springer, Berlin, Heidelberg, 2002).
[8] A. Luque and A. Martí, Phys. Rev. Lett. **78**, 5014 (1997).
[9] H. Y. Liu, M. Hopkinson, C. N. Harrison, M. J. Steer, R. Frith, I. R. Sellers, D. J. Mowbray, and M. S. Skolnick, J. Appl. Phys. **93**, 2931 (2003).
[10] S. Krishna, J. Phys. D **38**, 2142 (2005).
[11] A. Amtout, S. Raghavan, P. Rotella, G. von Winckel, A. Stintz, and S. Krishna, J. Appl. Phys. **96**, 3782 (2004).
[12] A. Stintz, G. T. Liu, H. Li, L. F. Lester, and K. J. Malloy, IEEE Photon. Technol. Lett. **12**, 591 (2000).
[13] X. D. Huang, A. Stintz, C. P. Hains, G. T. Liu, J. Cheng, and K. J. Malloy, IEEE Photon. Technol. Lett. **12**, 227 (2000).
[14] X. D. Xu, B. Sun, P. R. Berman, D. G. Steel, A. S. Bracker, D. Gammon, and L. J. Sham, Science **317**, 929 (2007).
[15] M. Kolarczik, N. Owschimikow, J. Korn, B. Lingnau, Y. Kaptan, D. Bimberg, E. Schöll, K. Lüdge, and U. Woggon, Nat. Commun. **4**, 2953 (2013).
[16] O. Karni, A. Capua, G. Eisenstein, V. Sichkovskyi, V. Ivanov, and J. P. Reithmaier, Opt. Express **21**, 26786 (2013).
[17] N. Tessler and G. Eisenstein, IEEE J. Quantum Electron. **29**, 1586 (1993).
[18] D. Gready and G. Eisenstein, IEEE J. Quantum Electron. **46**, 1611 (2010).
[19] M. Gioannini, A. P. Cédola, N. Di Santo, F. Bertazzi, and F. Cappelluti, IEEE J. Photovolt. **3**, 1271 (2013).
[20] T. F. Boggess, L. Zhang, D. G. Deppe, D. L. Huffaker, and C. Cao, Appl. Phys. Lett. **78**, 276 (2001).
[21] T. Müller, F. F. Schrey, G. Strasser, and K. Unterrainer, Appl. Phys. Lett. **83**, 3572 (2003).
[22] P. Dawson, O. Rubel, S. D. Baranovskii, K. Pierz, P. Thomas, and E. O. Göbel, Phys. Rev. B **72**, 235301 (2005).
[23] S. Sanguinetti, M. Henini, M. Grassi Alessi, M. Capizzi, P. Frigeri, and S. Franchi, Phys. Rev. B **60**, 8276 (1999).
[24] Z. C. Xu, K. Leosson, D. Birkedal, V. Lyssenko, J. M. Hvam, and J. Sadowski, Nanotechnol. **14**, 1259 (2003).
[25] C. Lobo, R. Leon, S. Marcinkevicius, W. Yang, P. C. Sercel, X. Z. Liao, J. Zou, and D. J. H. Cockayne, Phys. Rev. B **60**, 16647 (1999).
[26] H. D. Robinson, B. B. Goldberg, and J. L. Merz, Phys. Rev. B **64**, 075308 (2001).

[27] R. Oulton, J. J. Finley, A. I. Tartakovskii, D. J. Mowbray, M. S. Skolnick, M. Hopkinson, A. Vasanelli, R. Ferreira, and G. Bastard, Phys. Rev. B **68**, 235301 (2003).
[28] C.-I. Shih, C.-H. Lin, S.-C. Lin, T.-C. Lin, K. W. Sun, O. Voskoboynikov, C.-P. Lee, and Y.-W. Suen, Nanoscale Res. Lett. **6**, 409 (2011).
[29] Y. Toda, O. Moriwaki, M. Nishioka, and Y. Arakawa, Phys. Rev. Lett. **82**, 4114 (1999).
[30] H. Y. Liu *et al.*, J. Crystal Growth **210**, 451 (2000).
[31] M. Syperek, M. Baranowski, G. Sęk, J. Misiewicz, A. Löffler, S. Höfling, S. Reitzenstein, M. Kamp, and A. Forchel, Phys. Rev. B **87**, 125305 (2013).
[32] R. Ferreira and G. Bastard, Nanoscale Res. Lett. **1**, 120 (2006).
[33] S. C. Kuhn and M. Richter, Phys. Rev. B **90**, 125308 (2014).
[34] N. Owschimikow, M. Kolarczik, Y. I. Kaptan, N. B. Grosse, and U. Woggon, Appl. Phys. Lett. **105**, 101108 (2014).
[35] Y. Kaptan, H. Schmeckebier, B. Herzog, D. Arsenijević, M. Kolarczik, V. Mikhelashvili, N. Owschimikow, G. Eisenstein, D. Bimberg, and U. Woggon, Appl. Phys. Lett. **104**, 261108 (2014).
[36] E. Malic, M. Richter, G. Hartmann, J. Gomis-Bresco, U. Woggon, and A. Knorr, New J. Phys. **12**, 063012 (2010).
[37] J. Gomis-Bresco, S. Dommers, V. V. Temnov, U. Woggon, M. Laemmlin, D. Bimberg, E. Malic, M. Richter, E. Schöll, and A. Knorr, Phys. Rev. Lett. **101**, 256803 (2008).
[38] T. R. Nielsen, P. Gartner, and F. Jahnke, Phys. Rev. B **69**, 235314 (2004).
[39] S. Sanguinetti, T. Mano, M. Oshima, T. Tateno, M. Wakaki, and N. Koguchi, Appl. Phys. Lett. **81**, 3067 (2002).
[40] R. Ferreira and G. Bastard, Appl. Phys. Lett. **74**, 2818 (1999).
[41] I. O'Driscoll, T. Piwonski, C.-F. Schleussner, J. Houlihan, G. Huyet, and R. J. Manning, Appl. Phys. Lett. **91**, 071111 (2007).
[42] Y. I. Mazur, B. L. Liang, Z. M. Wang, D. Guzun, G. J. Salamo, Z. Y. Zhuchenko, and G. G. Tarasov, Appl. Phys. Lett. **89**, 151914 (2006).
[43] P. Borri, W. Langbein, U. Woggon, M. Schwab, M. Bayer, S. Fafard, Z. Wasilewski, and P. Hawrylak, Phys. Rev. Lett. **91**, 267401 (2003).
[44] L. Wang *et al.*, New J. Phys. **10**, 045010 (2008).
[45] K. Alavi, R. L. Aggarwal, and S. H. Groves, Phys. Rev. B. **21**, 1311 (1980).
[46] G. Visimberga, G. Rainò, A. Salhi, V. Tasco, M. T. Todaro, L. Martiradonna, M. De Giorgi, A. Passaseo, R. Cingolani, and M. De Vittorio, Appl. Phys. Lett. **93**, 151112 (2008).
[47] S. Stufler, P. Ester, A. Zrenner, and M. Bichler, Appl. Phys. Lett. **85**, 4202 (2004).
[48] K. J. Williams, R. D. Esman, and M. Dagenais, IEEE Photon. Technol. Lett. **6**, 639 (1994).